

A Design and Optimization of Multi-slot Diffusers for Power Augmentation in Small Axial Flow Wind Turbines

A. Naghavi Moghaddam¹, S. Malek Jafarian^{1†}, S. Mirbozorgi¹ and A. Bak Khoshnevis²

¹ Department of Mechanical Engineering, University of Birjand, Birjand, Iran

² Department of Mechanical Engineering, Hakim Sabzevari University, Sabzevar, Iran

†Corresponding Author. Email-address: mmjafarian@birjand.ac.ir

ABSTRACT

This study delves into a cutting-edge approach to boosting the efficiency of small urban wind turbines through the innovative use of power augmentation diffusers. Due to their compact size and the naturally low wind energy availability in urban areas, conventional small wind turbines often fall short in economic viability. Power augmentation, particularly using multi-slotted diffuser shrouds for boundary layer control (BLC), presents a promising solution. In this research various diffuser geometries are designed and tested using Ansys Fluent software and the SST k- ω turbulence model. The resulting data is integrated into an artificial neural network (ANN) and further optimized using both single-objective and multi-objective genetic algorithms (GA). Remarkably, the optimized designs demonstrate a significant increase in kinetic energy, with one geometry achieving nearly 5 times the free-stream kinetic energy at the throat and another delivering over 5.3 times more at the throat and 52% higher kinetic energy at the diffuser outlet. These breakthroughs offer valuable insights for the future of small wind turbine design, providing a pathway to more efficient, economically feasible solutions.

Article History

Received August 19, 2024

Revised December 30, 2024

Accepted January 4, 2025

Available online March 30, 2025

Keywords:

BLC diffuser

Optimization

Single-objective GA

Multi-objective GA

Flow separation

Airfoil

1. INTRODUCTION

Renewable technologies are considered clean sources of energy, and optimal use of these resources minimizes environmental impacts, produces minimum secondary wastes, and is sustainable based on current and future economic and social needs (Panwar et al., 2011). Wind energy technology has become one of the fastest growing energy sources in the world, and it symbolizes a feasible alternative, since it is a virtually endless resource. However, compared to the overall energy demand, the scale of wind power usage is still microscopic. As for the reasons for this matter, various causes are possible, for example, cost (Thangavelu et al., 2013). Perhaps it can be said that the current high cost of this clean and renewable energy is influenced by the low energy prices, and as a result, to obtain a significant amount of energy from the wind, various equipment and facilities are required. Based on existing relationships, the energy or total power available in the wind is proportional to the air density ρ , the cross-sectional area A , through which the flow passes, and the third power of free-stream velocity (Ackermann & Söder, 2002). It is important to note that the theoretical optimum for utilizing the power in the wind by reducing its speed was first discovered by Betz in 1926

(Ahmed, 2010). According to Betz findings, the maximum power that can be extracted from the wind is only 0.593 of the wind energy rate, and it is the optimal theoretical power (Ackermann & Söder, 2002). In practice, however, aerodynamic, mechanical, and electrical losses reduce the amount of extractable power, so the maximum power is only a fraction of the Betz limit (Wilson, 1980). Ultimately, the Betz limit is an idealization and a design goal that designers try to reach in a real-world turbine. A C_p value of between 0.35 – 0.40 is a realistic design goal for a practical wind turbine. This is still reduced by a capacity factor accounting for the periods of wind flow, as the intermittency factor (Magdi & Adam, 2011).

Based on calculations, the actual wind energy power for standard passing air with a density of ($\rho = 1.225 \text{ kg} / \text{m}^3$) and a velocity of ($u_\infty = 5 \text{ m} / \text{sec}$) from a circular surface, with a diameter of ($D = 1 \text{ m}$), taking into account the Betz limit, as well as approximate aerodynamic and mechanical losses, is approximately 25 Watts, which is not significant. In other words, the low energy density of wind and the costs of site operation and power collection imply that WECs for utility systems must be as large as possible. However, there are

NOMENCLATURE		Greek Symbols	
A	area	α	angle of attack
CD	Convergent Divergent	β, β^*, γ	coefficient in $k\omega$ model
C_B	chord of main diffuser	$\delta_{i,j}$	Kronecker's delta
C_P	power coefficient	ΔX	Airfoils Axial Overlap (AAO)
C_{PBetz}	betz power coefficient	ΔY	Airfoils Radial Distance (ARD)
C_S	chord of blc diffuser	θ_1, θ_2	angle of the diffuser converging/diverging section
D	throat diameter diffuser	κ	von Karman constant
$\dot{E}_{f,s(exit)}$	free stream rate of energy in exit area	μ, μ_t	dynamic molecular & eddy viscosity
$\dot{E}_{f,s(thr)}$	free stream rate of energy in throat area	ν, ν_t	laminar and turbulent eddy viscosities
\dot{E}_{Wind}	total wind rate of energy	ρ	density
$F_{1,2}$	model blending functions	$\sigma_{k,\omega}$	turbulent Schmidt number
K	total turbulent kinetic energy	τ_{ij}	turbulent stress tensor
L_1, L_2	length of the diffuser converging/diverging section	ω	specific turbulent dissipation rate
\dot{m}	mass flow rate	Acronyms	
P_{exit}	free-stream power at the outlet-equivalent area	<i>ANN</i>	Artificial Neural Network
P_{throat}	throat power enhancement	<i>AOA</i>	Angle of Attack
PA_{exit}	power augmentation in exit area	<i>BoI</i>	Body of Influence
PA_{throat}	power augmentation in throat area	<i>BL</i>	Boundary Layer
P_k	production rate of k	<i>BLC</i>	Boundary Layer Control
P_ω	production rate of ω	<i>CAWT</i>	Collector-Augmented Wind Turbine
Re	Reynolds number	<i>CDAWT</i>	Collector- and Diffuser-Augmented Wind Turbine
S_{ij}	mean strain rate tensor	<i>DAWT</i>	Diffuser-Augmented Wind Turbine
u_{aveAns}	Ansys computation of throat average velocity	<i>GA</i>	Genetic Algorithm
u_{aveGA}	GA predict of throat average velocity	<i>LSTM</i>	Long Short-Term Memory
u_i	velocity components (u, v, w) in cartesian directions: x, y, z	<i>MSE</i>	Mean Square Error
u_τ	friction velocity	<i>PA</i>	Power Augmentation
u_∞	free stream velocity	<i>RPD</i>	Relative Percentage Difference
y_{max}	maximum of the first bl height	<i>VA</i>	Velocity Augmentation
y^+	dimensionless wall distance $\left(\frac{u_\tau y}{\nu}\right)$	<i>WECS</i>	Wind Energy Conversion Systems

constraints on the size, and therefore power output of conventional WECSs that can be built and operated reliably (Gilbert & Foreman, 1979). In parallel with designing and constructing large wind turbines based on expanding the flow passage area and increasing power, there is a perspective emphasizing the augmentation of wind energy density. This viewpoint involves a general approach to wind turbine augmentation systems, using augmentative features such as nozzle and diffuser shrouds, or their combination. Such turbines are an optimized class of wind turbines that use a diffuser to accelerate and direct airflow onto a wind turbine rotor, to drive it for higher RPM and power output rather than without the diffuser. This power output is typically rated in terms of power augmentation (Agha et al., 2018). Essentially, the PA of wind turbines is carried out through four general methods: shrouded turbine, CAWT, DAWT, and CDAWT (Ghajar & Badr, 2008). The technique of augmenting wind turbines results from two fundamental concentrator mechanisms, which are increasing mass flow rate and wake mixing with the external flow (Alquraishi et al., 2019). The studies indicate that a ducted turbine consistently generates a higher power output compared to the bare turbine model. Ducts enhance flow turbulence

and blade trailing-edge vortices compared to the bare turbine.

However, they weaken the tip and hub vortices (Ding et al., 2022). Using power-augmenting nozzles facilitates the enhanced gathering and acceleration of wind (Mohammed et al., 2022). Increasing the mass flow rate is achieved by increasing the diffuser outlet area ratio and/or reducing the negative pressure behind the diffuser exit (Van Bussel, 2007). The beneficial influence on the recovery coefficient of pressure, base pressure, and increased flow velocity through the nozzle (Igra, 1981; Lawn, 2003), along with the improvement of the static pressure increase coefficient from the nozzle to the diffuser outlet (Dong et al., 2023), are among the advantages of power-enhancing shrouds. The possibility of automatically aligning the enhanced wind turbine array with the airflow in crosswinds (Ohya et al., 2008; Ohya & Karasudani, 2010) also arises.

Additionally, increased safety and protection of the turbine assembly, especially the blades, against collisions with external objects (Ohya et al., 2008; Ohya & Karasudani, 2010) could be highlighted. The ability to extract power higher than the free stream flow energy rate

at an equivalent level to the diffuser outlet and initiating turbine startup (Cut-in), consequently increasing the annual energy yield (Ranjbar et al., 2022), are additional achievements of power-enhancing shrouds. With the help of these shrouds, tip vortices are suppressed, leading to a reduction in turbine noise and sound emission (Abe et al., 2005, 2006). Instead of the near-tip (center) proximity, the possibility of extracting energy from the diffuser wall proximity (high speed/less torque) is provided (Abe et al., 2005; Tripathi, 2017). The use of high-efficiency diffusers transforms axial vortices in the rotor into circumferential vortices, which have a significant positive impact on the radial velocity gradients and assist in returning the flow to the desired axial state (Vaz & Wood, 2018). Ultimately, an increase in wind speed in the nozzle leads to an increase in turbine torque and power (Alquraishi et al., 2019).

Despite all the mentioned advantages of the diffuser, the positive pressure gradient in the diverging section and the associated challenges are a problem which needs addressing. When the overall divergence angle is around 7 to 10 degrees (Loeffler, 1981), the negative implications of this positive pressure gradient are minimal. However, in compact and short diffusers with a greater divergence angle, the flow tends to separate, and it may even reverse inside the diffuser, contrary to the desired direction. To address this issue, with the help of a tip and blade, the flow can be directed from the internal and central section towards the diffuser walls. Utilizing suction generated from the low-pressure region behind the flange or raised lip guides the flow outward. By injecting high-energy external flow and momentum in the desired direction into the low-energy boundary layer near the wall, the separation of flow and undesirable flows can be prevented (Shahsavari et al., 2015).

2. LITERATURE REVIEW

Since the 1930s, ducted turbines have garnered significant attention due to their potential for achieving higher power output compared to conventional turbines (Bontempo et al., 2021). Building on this, (Lilley & Rainbird, 1956) conducted research that demonstrated the strong dependence of the power amplification ratio on the diffuser outlet pressure coefficient. Their findings revealed that incorporating a flow amplifier at the diffuser outlet could substantially enhance power output (Oman et al., 1976b). gained valuable experience in controlling the boundary layer of divergent diffusers. They analyzed and tested two types of compact diffusers using a mesh screen to simulate turbines. They found that a conical diffuser with a 20° divergence half angle with two BLC tangential grooves provides a power amplification ratio of 1.7 at an area ratio of 2.8. In contrast, a double circular flap type diffuser at A level of 3.8 gives a power augmentation ratio of 2.1. (Igra, 1981) introduced the use of a circular flap or the BLC method to improve the performance of the power boost shroud and showed that by using a flap with an asymmetric generating airfoil of the NACA 4412 type, up to 80% improvement is obtained. The injection of external flow through the holes embedded in the wall of the rear part of the diffuser increases the power by about 25%. (Loeffler, 1981), investigated diffuser-enhanced wind

turbines with the tangential flow injection method, introduced through the slotted walls of the diverging section, to control the boundary layer. He concluded that using this method, the divergence angle of the diffuser can be between 60 and 80 degrees instead of the usual range of 7 to 10 degrees. In this way, the findings of (Oman et al., 1976a) were confirmed. (Gilbert & Foreman, 1983), continuing their previous research, showed how the additional momentum generated by the tangential injection of the free air flow helps the main flow to overpower frictional losses and prevent flow separation. They obtained a power amplification ratio of 4.25 in wind turbine which is reinforced with shroud, compared to the same wind turbine without shroud. Kwong and Dowling (1994) found that the axial flow injection is also useful in improving the pressure recovery of rectangular diffusers. They used two active control methods to reduce transient instability and retardation. According to their findings, a combination of stable and unstable blowing has a good average pressure recovery and reduces pressure fluctuations. In 1997, the first practical experience of designing and manufacturing diffuser-enhanced wind turbines on a commercial scale was done. This diffuser-enhanced wind turbine was named Vortec-7 and was based on the BLC (Phillips et al., 1999). They optimized Vortec-7. Their optimization was done, both in the turbine hub and in the power booster diffuser. In their optimizations, the inlet of the main diffuser was modified, and also by removing the protruding edge of the BLC diffuser, an overlap was created between the two diffusers. Phillips (2003) used an asymmetric airfoil cross-section to create the main diffuser and used another narrow airfoil cross-section for the second diffuser in order to control the boundary layer. In the other two designs, he first presented an innovative multi-slot BLC design, and in the next design, he also optimized it. Based on the findings, the maximum power amplification factor was 2.4. Ruprecht and Reinhardt (2003) developed a compact marine current turbine in which the concept of power enhancement by accelerating the boundary layer flow was well used. In their design, in addition to the main diffuser where turbine was located in its throat, an energetic flow was injected into the boundary layer in three stages and through the gaps between the diffusers. They selected the diameter of the throat as 20m and the diameter of the outlet of the diffuser as 30m and delayed the separation of the flow until 15m inside the diffuser. In 2014, (Ben David Wood, 2014), significantly improved the efficiency of wind turbines through the development of a power-boosting shroud. This innovative invention introduced key advancements that substantially enhanced both aerodynamic performance and energy capture. These improvements optimized airflow and increased overall efficiency by effectively managing air currents. Furthermore, Wood integrated aeroelastic materials that adaptively deform in response to variations in wind conditions. Hjort and Larsen (2014) presented a design of a three-layer composite diffuser using several curved diffusers. The strength of Their design was that in addition to the throat, where 64% more power is obtained than the Betz limit, the diffuser output is also 49% more than the Betz limit. Agha et al. (2018), while reviewing diffuser-enhanced wind turbine technologies, separately dealt with

BLC multi-slot diffusers. Among the advantages listed for multi-slot diffusers was the empowerment of the internal boundary layer of the diffuser, which is done with the help of circular flaps whose cross-sectional area provides high lift force. This action creates local velocity and pressure fields, which leads to more mass flow in the diffuser. According to their findings, the maximum power amplification factor in diffusers reinforced with shroud is between 2 and 3. [Koc and Yavuz \(2019\)](#) worked together in order to increase mass flow rate and the potential for generating more power. They focused on the effects of the main airfoil parameters and a circular control layer in the boundary layer. Using two-dimensional numerical fluid dynamics analysis, they designed experiments using a Box-Behnken design and response surface methodology to provide an optimal geometry. [Dighe et al. \(2019\)](#) investigated the effect of multi-element PA shrouds on the aerodynamic performance of wind turbines numerically. They found that in a PA shroud comprising a main diffuser and a circular control layer, increasing the radial gap size led to higher turbine thrust. In contrast, a larger deflection angle of the circular control element had the opposite effect. [García Auyanet and Verdin \(2022\)](#) designed and analyzed a DAWT with a multi-slot converging-diverging nozzle. The main goal was to perform three-dimensional numerical simulations of the multi-slot channel and evaluate the impact of the circular control layer geometry. It was determined that the thinner and more highly curved circular control elements produced higher PA.

A review of past researches indicates that continuous efforts have been made to economically harness wind power. In addition to constructing very large wind turbines, researchers have endeavored to make small-scale wind turbines efficient and justifiable through various power-enhancing methods. As mentioned, one effective method for power enhancement is directing the high-energy flow towards the boundary layer of the diverging diffuser section, resulting in boundary layer control. This leads to a controlled boundary layer by implementing a multi-stage divergence section, which in consequence allows the outer high-energy flow to enter the proximity of the inner diverging wall through gaps between diffusers. It guides the low-energy boundary layer flow, which tends to separate in the region with positive pressure gradient, in the desired direction through the diffuser gaps.

Although the effects of parameters related to the BLC section, such as gap width, divergence angle of the diffusers, the axial overlap and aspect ratio of two-stage diffusers, have been studied in a parametric investigation, there still exists a gap in comprehensive research on the design and optimization of the geometry of multi-stage BLC diffusers. It is essential to systematically and scientifically address this gap within the framework of a methodical approach, utilizing ANN and GA approaches. The goal is to derive a geometry that maximizes the throat velocity increase ratio with the minimum possible area ratio. These maximum throat velocities correspond to the highest kinetic energy extraction, and are entirely accessible for extracting the maximum power from small wind turbines.

In this regard, a set of BLC diffusers with randomly generated geometric parameters has been designed, where each set of diffusers has random axial overlap, radial gap, and divergence angle. These random parameters in other diffusers can vary within defined ranges. The numerical outputs of these geometries, obtained through Fluent simulation, have been used as inputs for an ANN, and the fitted outputs from the ANN have been used as inputs for a GA. Ultimately, the optimal geometry is obtained: a diffuser geometry that demonstrates remarkably high efficiency, and its rate of throat kinetic energy extraction is noteworthy.

3. METHODOLOGY

To achieve an optimal geometry, the diverging section of a converging-diverging BLC diffuser was designed at the start of this study using SolidWorks. A total of 120 CAD models were created using SolidWorks. Specifically, by selecting random parameters (within the defined constraints) for the divergence angle of the annular flaps, axial overlap, and their radial spacing from each other, initial 2D models were generated. These 2D models were then rotated around the axis of symmetry to generate the corresponding 3D models. Each model was subsequently imported into ANSYS individually, meshed appropriately, and solved using the ANSYS Fluent solver. The 3D solution domain was defined as a 30-degree cylindrical sector, several times larger than the dimensions of the diffuser, to reduce the number of mesh elements and facilitate mesh-independent solutions. Output results, such as the average throat velocity, throat energy rate, and other relevant parameters, were obtained and saved in an Excel file. Then, employing an ANN, the output of these geometry solutions is fitted based on the geometric parameters of the diffusers, representing the maximum throat velocity. Finally, utilizing a GA, the geometry of the diverging section is optimized in a way that maximizes the throat velocity within the geometry. Due to the fact that optimization has been conducted along two different paths, the objective functions differ. In the single-objective optimization, the selected objective function is the average throat velocity, which is to be maximized. In the multi-objective optimization, the objective functions are the average throat velocity and the diffuser exit-to-throat area ratio (also known as the area ratio), where the former is to be maximized and the latter minimized.

Building upon this approach, recent advancements in deep learning, such as the enhanced LSTM model, have been utilized to improve wind velocity prediction accuracy in turbine systems ([Ramesh Kumar & Selvaraj, 2023](#)). These models can complement traditional ANN and GA optimization techniques to further enhance the performance of wind systems.

3.1 Design and Geometric Specifications

In the initial section of the BLC diffuser, a diffuser with the cross-sectional profile FX69 PR281 from the Wortmann airfoil series has been employed. This diffuser comprises a convergent inlet, a throat, and the beginning of the divergent section. According to the results of studies by ([Agha et al., 2020](#)), this airfoil has a high power

enhancement coefficient. Additionally, considering the results of research by (Dighe et al., 2018) and (García Auyanet & Verdin, 2022), which indicate that excessive thickness has a negative impact on the efficiency of the diffuser, the airfoil thickness has been considered as 65% compared to the original airfoil. Accordingly, the thickness-to-chord ratio of the used airfoil in the main diffuser is 18.7%.

Since a large number of circular flaps, in addition to increasing the complexity of the assembly and control of components, also raise construction costs, the BLC section has been designed with four circular flaps. These flaps provide four external high-energy flow entry paths to the boundary layer following the placement shown in Fig.1.

In selecting the profile for the BLC section, the findings of (García Auyanet & Verdin, 2022) and (Dighe et al., 2018) have been utilized, which recommended a thin profile. These profiles generate higher power enhancement. Therefore, in this study, the NACA 0009 profile with a relative thickness of 50% has been used. The NACA 0009 airfoil, due to its symmetric design, is ideal for applications requiring balanced lift and drag, offering stable performance across various angles of attack. Its high lift-to-drag ratio within a specific angle of attack range makes it popular in aerodynamic research and engineering, reducing drag and enhancing lift, which aids in transferring high-energy flow to the low-energy boundary layer (Seeni, 2019).

As shown in Fig. 1a, the chord length of the diffuser section profile was set to 100 mm for both the initial section (C_B) and the BLC section (C_S) to ensure geometric consistency and ease of manufacturability. The throat diameter (D) of 200 mm was selected based on standard diffuser design practices and to maintain compatibility with the expected flow conditions, balancing flow velocity and pressure recovery. These design parameters were validated through preliminary numerical simulations, confirming their suitability for achieving the performance objectives.

3.1.1 Model Design

In this section, the diffusers' geometries were designed within a specified range of parameter changes, including divergence angle, axial overlap, and radial spacing between consecutive diffusers. Each design consists of 12 independent, randomly selected parameters. Setting the number of boundary layer control diffusers to four, each with adjustable parameters, creates four high-energy flow entry slots and strikes a balance between complexity, cost, efficiency, and aerodynamic effectiveness. Adding more stages would increase design complexity, costs, and the need for precise adjustments, often without substantial performance gains, potentially leading to an unstable design.

These parameters include four variables for the divergence angles (α_1 to α_4), four variables for their relative overlap ($\frac{\Delta X_1}{C_B}$ to $\frac{\Delta X_4}{C_B}$), and four variables for the

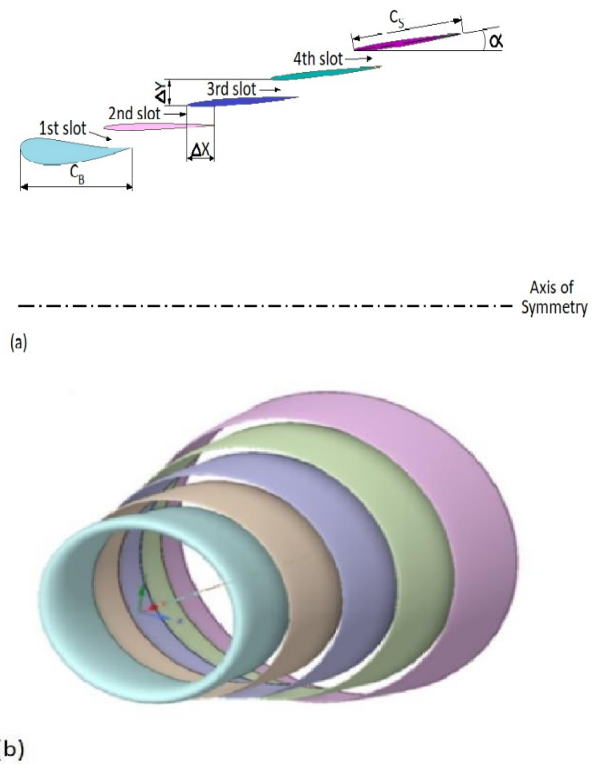


Fig. 1 Multi slot diffuser: (a) main parameters in 2D schematic; (b) 3D schematic

relative radial distance between the diffusers ($\frac{\Delta Y_1}{C_B}$ to $\frac{\Delta Y_4}{C_B}$).

The selected range for the divergence angles of the BLC diffusers is ($1^\circ \leq \alpha \leq 7^\circ$). Additionally, the relative axial overlap is considered ($0 \leq \frac{\Delta X}{C_B} \leq 0.5$) and the relative radial distance is assumed ($0.14 \leq \frac{\Delta Y}{C_B} \leq 0.2$). The rationale for selecting these ranges is to ensure that the exit-to-throat area ratio of the diffusers does not exceed 4, a defined ratio in studies related to enhancing power performance (Heyru & Bogale, 2022). In this paper, the 4:1 ratio is utilized due to its advantages in maintaining flow stability, reducing energy losses, and enhancing system efficiency, as confirmed by simulations under small wind turbine operating conditions (Jafari & Kosasih, 2014). Choosing larger surface ratios in diffusers necessitates the implementation of high divergence angles, which can increase the adverse pressure gradient and lead to reduced diffuser efficiency, a lower ideal pressure recovery coefficient, and increased entropy generation resulting from viscous and turbulent (Yadegari, 2021; Yadegari & Bak Khoshnevis, 2020a, b, c, 2021).

3.2 Governing Equation and Numerical Solution Method

The current problem was assumed to be steady, turbulent, incompressible, and three-dimensional. The governing equations that illustrate the present problem are continuity and momentum.

Continuity equation:

$$\frac{d\rho}{dt} + \rho \frac{\partial u_i}{\partial x_i} = 0 \quad (1)$$

Momentum equations:

$$\rho \frac{du_i}{dt} = -\frac{\partial p}{\partial x_i} + \frac{\partial}{\partial x_j} \left(2\mu S_{ij} - \frac{2}{3}\mu \frac{\partial u_k}{\partial x_k} \delta_{ij} - \rho \overline{u'_i u'_j} \right) \quad (2)$$

And

$$\rho \overline{u'_i u'_j} = -\mu_t \left(\frac{\partial \bar{u}_i}{\partial x_j} + \frac{\partial \bar{u}_j}{\partial x_i} \right) + \frac{1}{3} \rho \delta_{ij} \overline{u'_k u'_k} \quad (3)$$

And

$$S_{ij} = \frac{1}{2} \left(\frac{\partial u_i}{\partial x_j} + \frac{\partial u_j}{\partial x_i} \right) \quad (4)$$

In Eq. (2), $(-\rho \overline{u'_i u'_j})$ denotes Reynolds stresses. p , u_i , and u'_i , denotes mean static pressure, mean velocity and turbulent fluctuation respectively (Promthaisong & Eiamsa-ard, 2019; Ramayee & Supradeepan, 2022).

Transport equations for turbulent kinetic energy and specific rate of dissipation for SST k - ω turbulent model are as follows:

k – equation:

$$\frac{D(\rho k)}{Dt} = \frac{\partial}{\partial x_j} \left[(\mu + \sigma_k \mu_t) \frac{\partial k}{\partial x_j} \right] + \tilde{P}_k - \rho \beta^* k \omega \quad (5)$$

ω – equation:

$$\begin{aligned} \frac{D(\rho \omega)}{Dt} &= \frac{\partial}{\partial x_j} \left[(\mu + \sigma_\omega \mu_t) \frac{\partial \omega}{\partial x_j} \right] - \rho \beta \omega^2 + \frac{\gamma}{\hat{v}_t} P_k \\ &+ 2(1 - F_1) \rho \sigma_{\omega 2} \frac{1}{\omega} \frac{\partial k}{\partial x_i} \frac{\partial \omega}{\partial x_i} \end{aligned} \quad (6)$$

On the other hand

$$v_t = \frac{\mu_t}{\rho} = \frac{a_1 k}{\max(a_1 \omega, S F_2)} \quad (7)$$

Where $a_1 = 0.31$ and $S = \sqrt{S_{ij} S_{ij}}$ is the absolute value of the mean strain–rate tensor

And

$$F_2 = \tanh \left[\left\{ \max \left(\frac{2\sqrt{k}}{\beta^* \omega^2}, \frac{500\nu}{\omega y^2} \right) \right\}^2 \right] \quad (8)$$

And

$$\hat{v}_t = \max\{v_t, 10^{-8}\} \quad (9)$$

And the production terms are:

$$\tilde{P}_k = \min\{P_k, 10\beta^* \rho k \omega\} \quad (10)$$

Where the production term $P_k = \tau_{ij} \left(\frac{\partial u_i}{\partial x_j} \right)$ and the Reynolds stresses τ_{ij} are related to the mean strain–rate tensor S_{ij} through the Boussinesq approximation:

$$\tau_{ij} = 2\mu_t \left(S_{ij} - \frac{1}{3} S_{kk} \delta_{ij} \right) - \frac{2}{3} \rho k \delta_{ij} \quad (11)$$

Where δ_{ij} is Kronecker's delta.

Other parameters of model are:

$$P_\omega = \gamma \frac{P_k}{v_t} \quad (12)$$

$$F_1 = \tanh(\xi^4) \quad (13)$$

And

$$\xi = \min \left[\max \left\{ \frac{\sqrt{k}}{\beta^* \omega y}, \frac{500\nu}{\omega y^2} \right\}, \frac{4\sigma_{\omega 2} k}{CD_\omega y^2} \right] \quad (14)$$

$$CD_\omega = \max \left(\frac{2\sigma_{\omega 2}}{\omega} \frac{\partial k}{\partial x_i} \frac{\partial \omega}{\partial x_i}, 10^{-10} \text{sec}^{-2} \right) \quad (15)$$

It can also be expressed as:

$$(\sigma_k \sigma_\omega \beta)^T = F_1 (\sigma_k \sigma_\omega \beta)_1^T + (1 - F_1) (\sigma_k \sigma_\omega \beta)_2^T \quad (16)$$

With the following values:

$$\sigma_{k1} = 0.85, \quad \sigma_{\omega 1} = 0.5, \quad \beta_1 = 0.07$$

$$\sigma_{k2} = 1.0, \quad \sigma_{\omega 2} = 0.856, \quad \beta_2 = 0.0827$$

The coefficient γ is calculated from:

$$\gamma = \frac{\beta}{\beta^*} - \frac{\kappa^2}{\sigma_\omega \sqrt{\beta}} \quad (17)$$

with $\kappa = 0.41$ and $\beta = 0.09$.

The blending functions F_1 and F_2 in the context of the $k\omega$ turbulence model, particularly the Shear-Stress Transport (SST) model F_1 is designed to be 1 in the near-wall region, while F_2 equals 1 for boundary layer flows. Both functions use wall-distance for accurate formulation in the near-wall region and free-stream dependence in the outer part of the boundary layer, a key feature of the SST model. The text highlights the importance of eddy-viscosity modification to prevent non-physical behavior, especially in regions with strong pressure gradient (Menter, 1994, Menter et al. 2003; Goldberg & Batten, 2015; Rahman et al., 2019). These equations, after discretization by ANSYS Fluent and applying boundary conditions, have been numerically solved using the coupled pressure-velocity method.

3.3 Numerical Remark

The numerical solution for all geometries was performed in three dimensions within a domain as shown in Fig. 2. Due to the symmetry of the field, the reduction in the number of network elements, the decrease in computation time for each stage, and the ease of reaching an independent solution from the network, a 30-degree sector of the entire cylindrical domain is taken into consideration. The Reynolds number (Re) used in the numerical solution is 3.33×10^4 (based on the free-stream velocity ($u_\infty = 5 \text{ m/sec}$) and the cord length ($C_B = 0.1 \text{ m}$) for each of the diffusers). A wind speed of 5 m/s is commonly used in wind turbine research because it reflects average real-world conditions, exceeds the cut-in speed for most turbines, and allows for steady aerodynamic testing without excessive turbulence. This moderate speed serves as an effective baseline for energy yield estimation and efficiency evaluation, making it a standard choice for performance assessments in various studies (Zhang & Wang, 2023).

With the goal of $y^+ \leq 1$, the element sizes in the grid, as well as the exceptional compactness of the grid near the diffuser walls, have been selected in such a way that in different sections of the surface, the height of the first element or the first layer of the mesh is $5.5 \times 10^{-6} \text{ m}$ at the

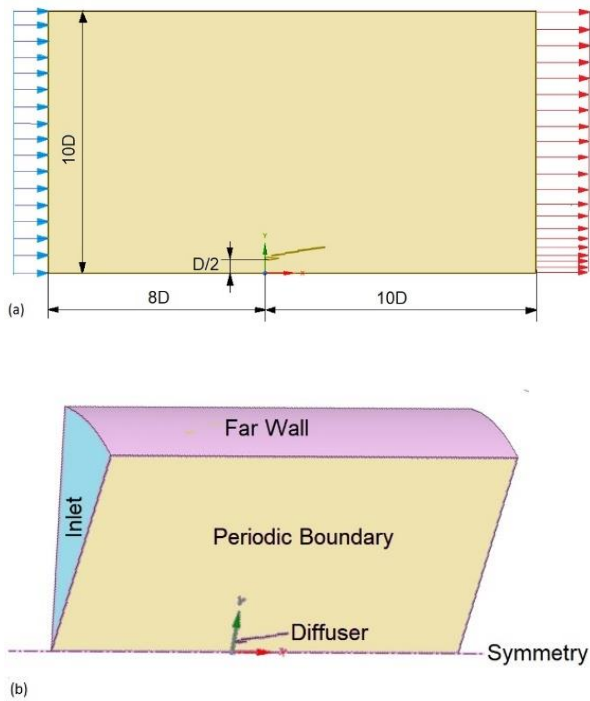


Fig. 2 Schematic of the computing domain: a) Two-dimensional; b) Three-dimensional

location of severe bending of the leading edge and sharp trailing edge. In other points of the diffuser, it is $1.1 \times 10^{-5} m$. In this way, y^+ between 0.14 to 0.28 is obtained, which is an appropriate value. The two-dimensional dimensions of the field under investigation were also selected, similar to the work of (Kishore et al., 2013) (see Fig. 2a), and transformed into three dimensions (see Fig. 2b). The dimensions of this field are 10 times the throat diameter radially and 18 times the throat diameter axially (Fig. 2a). In this way, the upper part of the diffuser has a length equivalent to 8 times the throat diameter. The remaining length of the field, from the diffuser inlet to the end of the field, is 10 times the throat diameter.

For simulating turbulence, the turbulence model $SST - k\omega$ has been used. This model can provide relatively accurate results in the heat transfer and displacement in arrays of swirling and impinging jets (Bode et al., 2020). Although the topic of heat transfer is not discussed in this research, the incoming flow from the control layer boundary slots behaves similarly to direct impingement jets. Therefore, the selection of this turbulence model is appropriate. This model is found to be superior in terms of prediction accuracy compared to other traditional turbulence models (Bode et al., 2020).

In order to achieve an appropriate numerical solution, it is necessary to investigate regions of the flow field that are more sensitive with a finer and more suitable mesh. This is addressed in the form of the BoI. In other words, the BoI pertains to domain regions with higher velocity gradients, which require a finer mesh (Tacutu et al., 2019). Therefore, three BoI. have been selected in order of importance: the inner and outer parts of the diffuser assembly, the region opposite the diffuser upstream and downstream, and the upper parts of the diffuser. The inner

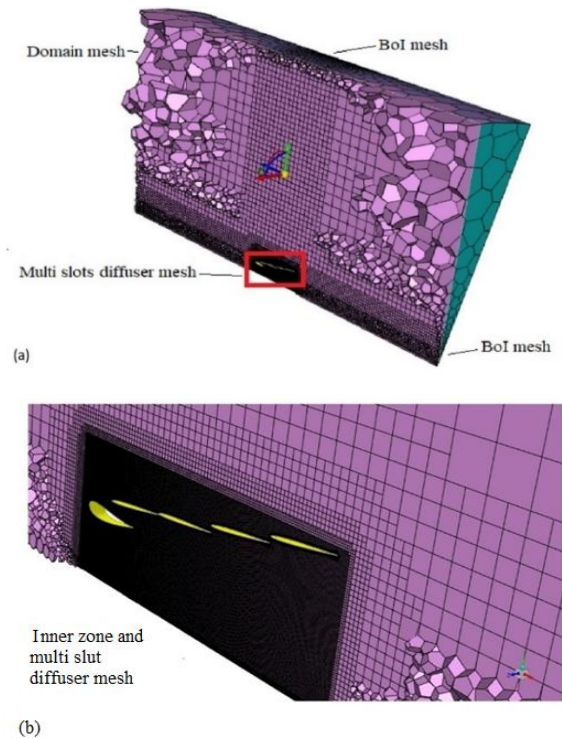


Fig. 3 Poly-hexcore mosaic mesh: (a) Total domain; (b) Inner zone mesh

and outer parts of the diffuser have a particularly fine mesh.

The mesh generated by the poly-hexcore technique has fewer number of grids and higher grid quality than other unstructured mesh, such as tetrahedral mesh. For selecting the flow solver, Ansys Fluent (with Fluent Meshing) was used. The advantage of choosing this solver is the utilization of polyhedral meshing. The mesh generated by the poly-hexcore technique has less number of grids and higher grid quality than other unstructured mesh, such as tetrahedral mesh (Mei et al., 2022). Fluent meshing is a mosaic mesh technology that automatically connects any mesh element to any other mesh element while maintaining compatibility (see Fig. 3). This meshing method connects high-quality octree hexahedron in the bulk region, and isotropic poly prisms in the boundary layer with the mosaic polyhedral elements. This results in an approximately 20 to 50% reduction in the total element count compared to the conventional hexcore mesh. That consequently speeds up the ANSYS Fluent solver by 10 to 50%, depending upon the application (Zore et al., 2019).

Although Hypermesh is suitable for meshing, ANSYS Fluent is often preferred for its superior performance and efficiency in fluid dynamics simulations. The integration of Fluent Meshing enhances these capabilities, making it a more effective choice for accurate results in complex analyses. When comparing the meshing techniques of Hypermesh and poly-hexcore, it is evident that poly-hexcore typically achieves better convergence speeds and requires fewer elements due to its structured nature. While Hypermesh can handle more complex geometries, it often needs a larger number of elements, making poly-hexcore a more efficient choice overall. Furthermore, although other software like Hypermesh has meshing capabilities,

ANSYS Fluent especially when used with Fluent Meshing is preferable for its enhanced performance and efficiency.

In order to accurately check the proximity of the solid walls in the growth range of the boundary layer, it is necessary to use a very fine mesh that grows slowly and is connected to the mesh outside the boundary layer. The internal boundary layer consists of three regions: the viscous sublayer, the buffer layer, and the logarithmic layer. The logarithmic layer is shared between the inner and outer regions. Under the viscous sublayer, the value of y^+ is equal to ($0 < y^+ < 5$) (Perlin et al., 2016). As a result, choosing a distance of 5 to 10 microns for the first boundary layer and $0.14 \leq y^+ \leq 0.28$ means that several layers of mesh are placed in the viscous sublayer, which is quite desirable.

3.4 Optimization of the Diffuser Design

In order to obtain an optimal geometry, two optimization methods are used. The first method is the gradient descent method, in which the change in the value of each variable is calculated using partial derivatives of the objective function concerning the design variables to optimize the function. Using this method requires adjusting the learning rate, which must be done through trial and error. If the learning rate is too high, the algorithm may jump past the optimal point, and if it is too low, it may require a large number of iterations, in which case the optimization process may take hundreds of hours. Therefore, the use of this method was ruled out. The alternative optimization method involves solving multiple geometries with random parameters and then using a neural network and GA. In this study, the second method was used, so an appropriate statistical population of 120 geometries was provided. In fact, 120 cases represent the minimum number of geometries obtained through the application of the neural network and genetic algorithm processes, which, after being modeled in SolidWorks and solved numerically in Fluent, yielded acceptable results, with the relative difference percentage (RPD) reaching approximately 2% or less. It should be noted that all 120 models were designed with randomly selected geometric parameters (within the defined constraints) for the divergence angle of the annular flaps, axial overlap, and their radial spacing from each other and were analyzed numerically using ANSYS Fluent software. ANSYS Fluent, particularly with Fluent Meshing, excels in numerical simulation due to its high-quality mesh generation, advanced solver capabilities, and extensive turbulence models. Compared to alternatives like OpenFOAM and COMSOL Multiphysics, Fluent offers superior accuracy and ease of use for wind turbine simulations, making it the optimal choice for performance-enhancing applications. Considering the direct and positive impact of BLC on flow conditions such as mass flow rate and maximum throat velocity, the optimal geometry is expected to have the highest throat velocity.

Additionally, the ratio of exit area to throat area, which results from selecting geometric parameters in the design, was also recorded. In this way, a matrix was obtained that

contains the output information. Another matrix serves as input data, where each row contains 12 randomly selected data points, including four angles of divergence, four axial overlaps, and four radial distances between the diffusers. In the single objective optimization case (GA), the output matrix includes the average throat velocity and the outlet area to throat area ratio. In the multi objective optimization case, the output consists of a column of 120 average throat velocities.

3.4.1 Artificial Neural Network

In this study, Artificial Neural Networks (ANN) were utilized to predict the outcomes of the optimization process. Among the various types of ANNs, the Multilayer Perceptron (MLP) was selected due to its proven effectiveness in handling complex optimization tasks. The MLP represents a category of artificial neural networks characterized by the presence of a minimum of one input layer, one or more hidden layers, and one output layer. This structured network operates by processing data through interconnected neurons. The MLP leverages the backpropagation algorithm to facilitate training and weight updates, thereby enhancing its capacity to decipher intricate and nonlinear patterns. Through the utilization of nonlinear activation functions such as sigmoid or ReLU, the MLP demonstrates the capability to approximate nearly any continuous function with a specified level of accuracy. These attributes, in conjunction with the adaptability to modify the quantity of layers and neurons, position the MLP as a potent instrument within the realm of machine learning and artificial intelligence (Hornik et al., 1989)

Building on these capabilities, the study employs the MLP model to accurately relate input parameters to desired output results, with the network demonstrating superior predictive power over traditional regression methods (Li et al., 2001; Siavash et al., 2021). For this purpose, MATLAB software has been utilized to implement an application for adapting the neural network data. The operation of this method is such that the neural network is trained with a large number of data obtained from solving the flow in different geometries within the solution domain (in this research, 120 cases). It can predict the flow behavior in different conditions based on the initial training. In this way, in the data selection section, input and output matrices were entered, and the input information for training, validation, and testing was divided. As the optimization is based on ANN, the network must be trained effectively so that in subsequent stages, the results of GA optimization can be improved.

3.4.2 Genetic Algorithm

The Genetic Algorithm (GA) is an optimization technique inspired by natural evolution, designed to solve complex problems through a process resembling selection, crossover, and mutation. In single-objective GA, the algorithm seeks to optimize a single objective function. However, in multi-objective GA, it generates a set of optimal solutions known as the Pareto front, balancing conflicting objectives. This approach is highly useful in multi-criteria decision-making (Konak et al., 2006).

3.4.2.1 Single Objective Genetic Algorithm:

The single objective genetic algorithm, drawing inspiration from biological principles, serves as an optimization technique employed to identify the optimal or most favorable solution to a range of complex problems. The algorithm comprises several key steps: initially, a set of potential solutions (referred to as chromosomes) is created through a random process. Subsequently, through the application of selection, crossover, and mutation operations, a new generation of solutions is generated. Each iteration involves the assessment of solutions based on a fitness function, with the top-performing solutions being retained for the subsequent generation. This iterative process persists until a specific termination criterion is achieved, such as reaching a defined number of generations or attaining a solution of sufficient fitness. Through this systematic approach, the algorithm progressively guides the population towards the optimal solution (Schmitt, 2001).

3.4.2.2 Multi Objective Genetic Algorithm:

The multi-objective genetic algorithm (GA) is a sophisticated optimization approach that extends the principles of the traditional GA to tackle complex problems with multiple, often conflicting objectives. This algorithm seeks Pareto-optimal solutions, which provide a range of trade-offs to suit diverse needs without one solution dominating others. By simultaneously evaluating and evolving solutions across multiple objective functions, the multi-objective GA enables the exploration of varied possibilities and identifies a set of high-quality solutions that represent the best compromise across all objectives. This approach allows for a comprehensive decision-making process, especially valuable in dynamic, multifaceted environments where single-objective optimization may be insufficient (Konak et al., 2006).

To further refine the solution accuracy within this multi-objective framework, an artificial neural network (ANN) was employed as an effective function approximator (Eriksson et al., 2022). By training the ANN in a way that closely approximates the output values in relation to the targets, a minimal mean squared error (MSE) was achieved, allowing for highly accurate predictions. This predictive capability means that even without the computational cost of solving each geometry numerically, the ANN can estimate results across the range of allowable geometric parameters, significantly accelerating the optimization process.

In this study, a multi-objective GA was used to maximize both the objective function and the average throat velocity while minimizing the exit area ratio. Alternatively, when prioritizing only the maximization of throat velocity, a single-objective GA was employed. Optimization using a single-objective GA involves encoding the objective function, selecting individuals based on a fitness criterion, and iteratively refining the population through mating and mutation operations. This iterative process continues until a stopping criterion is met, culminating in decoding to obtain optimized results (Pajasmaa et al., 2023). The integration of both multi-objective and single-objective GAs demonstrates the

adaptability of genetic algorithms, while the predictive capabilities of the ANN further enhance optimization efficiency.

4. NUMERICAL SOLUTION VERIFICATION

To ensure the accuracy of the numerical settings, a portion of the results has been referenced from an experimental numerical study (Kishore et al., 2013). In that study, a similar geometry was modeled using SolidWorks, and a poly-hexcore mesh was employed to obtain a three-dimensional solution.

Kishore et al. (2013) conducted a numerical solution for a simple converging-diverging diffuser in a two-dimensional axisymmetric flow and ultimately fabricated it. Given that the numerical solution in the present study exhibits a relative difference of less than 2.1% compared to Ali's results, the validity of the numerical settings for the geometry design is confidently supported.

In this study, three-dimensional modeling was employed to fully utilize the capabilities of Fluent meshing, particularly the advantages offered by polyhedral mosaic meshes, which enhance computational accuracy and efficiency. Even after incorporating three-dimensional flow dynamics and introducing perturbations to emulate realistic flow conditions, the numerical results remained consistent, with negligible error percentages observed. The solution field of the multi-slot boundary layer control diffuser was designed and optimized using appropriate software settings. To ensure the accuracy of the results, a comparative analysis was performed between our numerical findings and the numerical and experimental data from a reputable study, which validated the robustness of the proposed approach.

As (Kishore et al., 2013) analyzed various geometries, focusing on the effects of a convergent length of ($L_1 = 0.5D$) and a half-cone convergence angle of θ_1 on the throat velocity augmentation coefficient ($\frac{u}{u_\infty}$) while maintaining a constant divergent length of ($L_2 = 1.5D$) and a half-cone divergence angle of ($\theta_2 = 10^\circ$), the present study also modeled and performed numerical analysis on this geometry in three dimensions. Figure 4a depicts the two solutions (two-dimensional results from (Kishore et al., 2013) and the present study). According to Fig. 4a, the average RPD obtained is 2.3%, which is acceptable in engineering calculations. By comparing the results of the present three-dimensional numerical solution with the two-dimensional solution of the geometry in the study by (Kishore et al., 2013), the accuracy of the numerical solution was confirmed. Therefore, with similar and proportional settings to the desired flow field, the numerical solution of the geometries was performed.

In addition to comparing the numerical results of the throat velocity enhancement ratio with those reported by Kishore et al. (2013), the study also examined the relative power enhancement for their optimized geometry in three-dimensional flow using a poly-hexcore mesh. These results were compared with the two-dimensional solutions

Table 1 Comparison of power augmentation ratios between the numerical and experimental results from (Kishore et al., 2013) and the present study, including relative percentage differences (RPD)

Free stream velocity (u_∞)	Power augmentation results (Kishore et al., 2013) ($\frac{P_{throat}}{P_{exit}}$)		Numerical verification of PA in present study	RPD (%)	
	Numerical results	Experimental results		To Numerical results	To Experimental results
2.7	1.45	1.40	1.50	3.4	6.9
3.2	1.50	1.44	1.49	0.7	3.4
4.0	1.49	1.42	1.49	0	4.8
5.0	1.51	1.47	1.49	1.3	1.4

Table 2 Geometry parameters of the proposed single objective GA optimization

Divergence of BLC diffusers(deg)	α_1	α_2	α_3	α_4
	6.999	4.750	7.000	7.000
Axial overlap of BLC diffusers	$\frac{\Delta X_1}{C_B}$	$\frac{\Delta X_2}{C_B}$	$\frac{\Delta X_3}{C_B}$	$\frac{\Delta X_4}{C_B}$
	0.495	0.002	0.005	0.003
Radial distance of BLC diffusers	$\frac{\Delta R_1}{C_B}$	$\frac{\Delta R_2}{C_B}$	$\frac{\Delta R_3}{C_B}$	$\frac{\Delta R_4}{C_B}$
	0.200	0.140	0.170	0.200

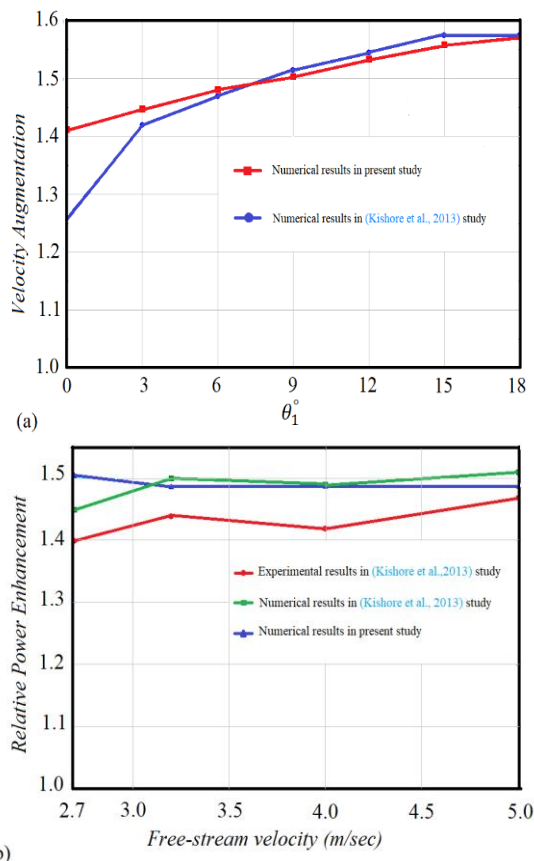


Fig. 4 Comparison of diffuser performance based on the results of this study and (Kishore et al., 2013): (a) Velocity ratio versus nozzle convergence angle θ_1 ; (b) Relative power enhancement at different free-stream velocity

provided in their study at four different speeds, as illustrated in Fig. 4b. and Table 1. Considering the contents of the table and the figure presented, a good agreement is observed between the numerical and

experimental results of the study, part of which has been verified, and the numerical results of the present study.

5. RESULTS AND DISCUSSION

The accuracy of the fitted functions in the ANN, including train, test and overall data, is illustrated in Fig. 5. In all parts of Fig. 5, the output obtained from the fitted functions closely matches the target values with minimal errors, which is agreeable. The MSE is also kept very low, indicating good agreement between the model and the data. In this study, a multi-layer perceptron ANN with 10 hidden layers was selected, and the Bayesian regularization algorithm was taken into consideration.

The output of the ANN was provided to a single-objective optimizer (GA) as input, with the fitness function as the output. The upper and lower constraints for the variables were selected according to the values specified in sections 3-1. The population size was set to 200, and the function tolerance was $1e-7$. A population size of 200 has been utilized in other studies and is considered a scientific and logical choice (Behzadian et al., 2009). In general, for a problem with 12 input variables, 2 output variables, and 120 states, a population size of approximately 200 is considered a suitable starting point. However, if optimal results are not achieved during the optimization process or if there is insufficient population diversity, it may be necessary to increase the population size. In this context, such a choice strikes a balance between optimization accuracy and the required time, making it appropriate for the problem at hand. This careful consideration of population size lays the groundwork for further analysis. Among the plotting functions, the best fitting function was selected (see Fig. 6). In this case, only one optimal geometry was obtained, in which the highest average throat velocity was the same as the one predicted by the single-objective GA (see Fig. 7 and Tables 2, 3). The mass flow rates of input and output flows were also presented in Table 4.

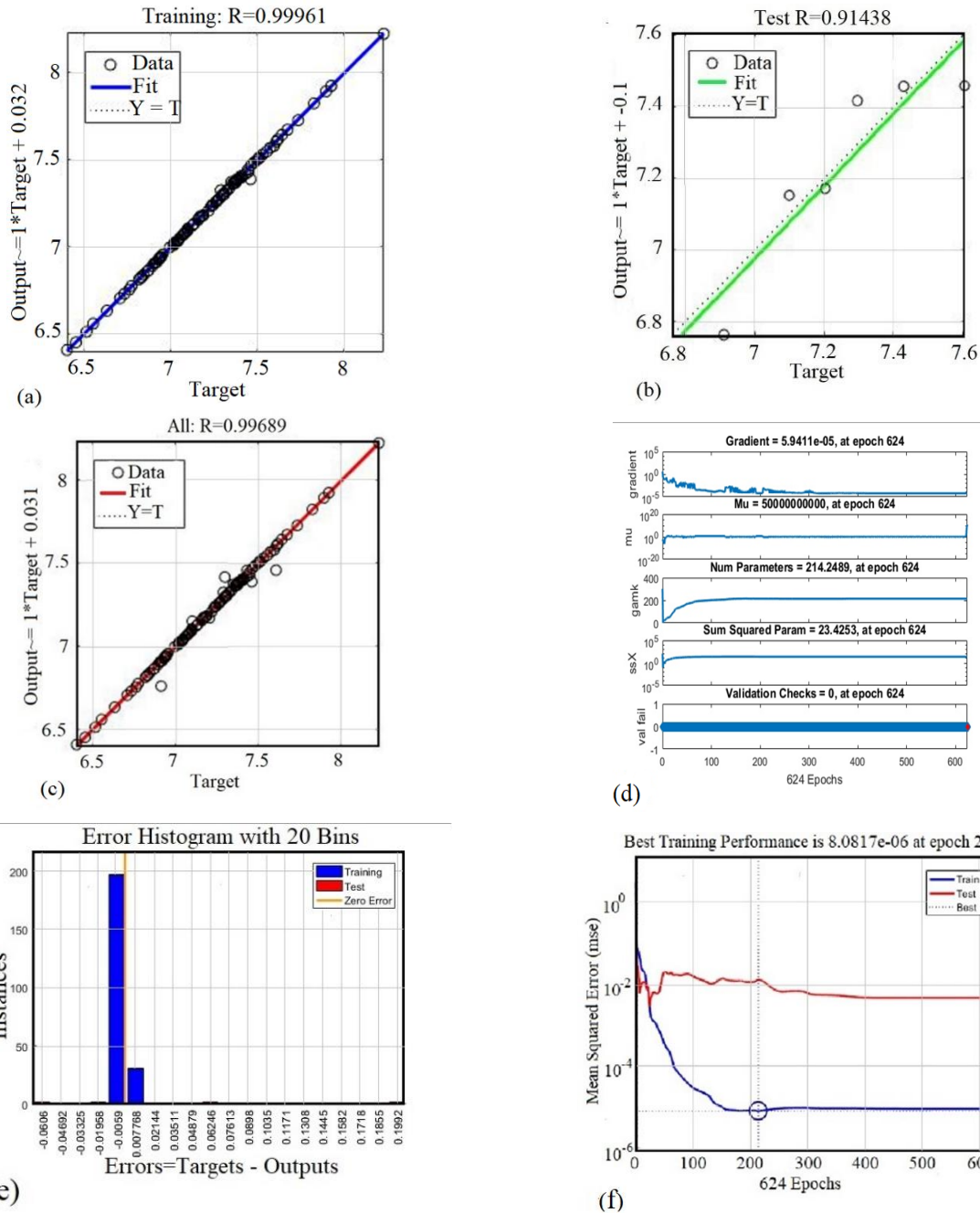


Fig. 5 ANN performance based on single-objective optimization for: (a) Training data; (b) Test data; (c) All data; (d) Training state; (e) Error histogram; (f) Best training performance

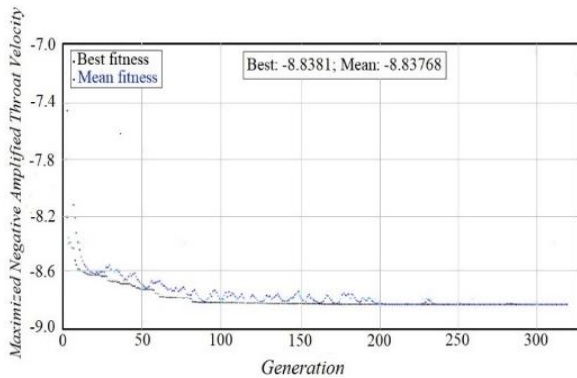


Fig. 6 Best fitness in single-objective optimization

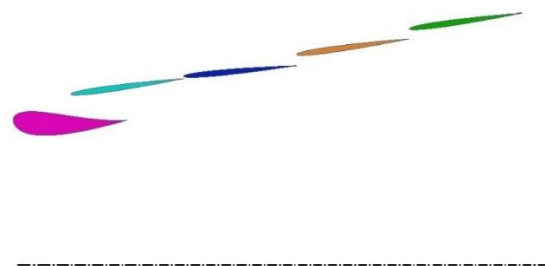


Fig. 7 Single objective GA optimized geometry

Table 3 Diffuser efficiency optimized with the single objective GA optimization

Freestream, throat velocities (ANSYS & GA Prediction), and RPD	$u_{\infty}(m/sec)$	$u_{ave_{Ans}}(m/sec)$	RPD (%)	$u_{ave_{GA}}(m/sec)$
	5	8.653	2.1	8.838
Mass and energy rate specifications	$\dot{m}_{throat}(kg/sec)$	$\dot{E}_{throat}(J/sec)$	$\dot{E}_{f.s.(exit)}(J/sec)$	$\dot{E}_{f.s.(thr.)}(J/sec)$
	0.333	12.853	9.157	2.405
The ratio of area, speed increase, and energy	Area ratio	PA_{throat}	PA_{exit}	VA
	3.810	5.344	1.404	1.7306

Table 4 Mass flow rate in the geometry optimized with a single objective GA

$\dot{m}(kg/sec)$					
Inlet	1st _{slot}	2nd _{slot}	3rd _{slot}	4th _{slot}	Outlet
0.333	0.107	0.007	0.060	0.052	0.559

Table 5 Geometry parameters of the proposed multi objective GA optimization

Divergence of BLC diffusers(deg)	α_1	α_2	α_3	α_4
	6.95	6.83	6.98	3.51
Axial overlap of BLC diffusers	$\frac{\Delta X_1}{C_B}$	$\frac{\Delta X_2}{C_B}$	$\frac{\Delta X_3}{C_B}$	$\frac{\Delta X_4}{C_B}$
	0.003	0.016	0.296	0.101
Radial distance of BLC diffusers	$\frac{\Delta R_1}{C_B}$	$\frac{\Delta R_2}{C_B}$	$\frac{\Delta R_3}{C_B}$	$\frac{\Delta R_4}{C_B}$
	0.163	0.140	0.143	0.161

Table 6 Diffuser efficiency optimized with the multi-objective optimization

Freestream, throat velocities (ANSYS & GA Prediction), and RPD	$u_{\infty}(m/sec)$	$u_{ave_{Ans}}(m/sec)$	RPD (%)	$u_{ave_{GA}}(m/sec)$
	5	8.401	1.6	8.271
Mass and energy rate specifications	$\dot{m}_{throat}(kg/sec)$	$\dot{E}_{throat}(J/sec)$	$\dot{E}_{f.s.(exit)}(J/sec)$	$\dot{E}_{f.s.(thr.)}(J/sec)$
	0.323	11.744	7.057	2.405
The ratio of area, speed increase, and energy	Area ratio	PA_{throat}	PA_{exit}	VA
	3.205	4.883	1.524	1.6802

In the second part of this study, the ANN was once again employed in order to maximize the average throat velocity and minimize the exit-to-throat area ratio. In this case, the output of the ANN illustrates high accuracy as well in the process (see Fig. 8). In all parts of Fig. 8, the output obtained from the fitted functions closely matches the target values with minimal errors which is agreeable. The MSE is kept very low, indicating good agreement between the model and the data. In this section, a multi-layer perceptron ANN with ten hidden layers was also selected, and the Bayesian regularization algorithm was used. The Bayesian regularization algorithm in Artificial Neural Networks (ANN) improves model accuracy by integrating prior knowledge, constrains model complexity to prevent overfitting, and enhances generalization to new data. It also quantifies prediction uncertainty, adding value in decision-making. Overall, Bayesian regularization boosts the robustness and reliability of ANN models across applications.

The output of an artificial neural network was utilized as input for a multi-objective GA. For this purpose, 12 variables and constraints as described in sections 3-1 are used. The population size was set to 200, the optimization stop criterion was set to satisfy a function tolerance of 1e-

6, and the Pareto front was selected as the plot function showing a spectrum of optimal states. Since all points between the coordinate axes and the Pareto front especially the ideal origin coordinates are inaccessible, the best point is the closest point to the origin. In Fig. 9, the information of the Pareto front along with the information obtained from the initial geometries, and in Fig. 10, the geometry of the optimized diffuser at the best point which is the closest to the ideal point, is shown with \blacklozenge . This multi-objective optimization provides the maximum throat velocity augmentation with the minimum area ratio. The parameters of this optimized geometry are presented in Table 5, and its performance is also indicated in Table 6. Additionally, the mass flow rates at the inlet and outlet of the multi-objective optimized diffuser are displayed in Table 7.

Table 7 Mass flow rate in the geometry optimized with a multi-objective GA

$\dot{m}(kg/sec)$					
Inlet	1st _{slot}	2nd _{slot}	3rd _{slot}	4th _{slot}	Outlet
0.323	0.096	0.006	0.019	0.013	0.457

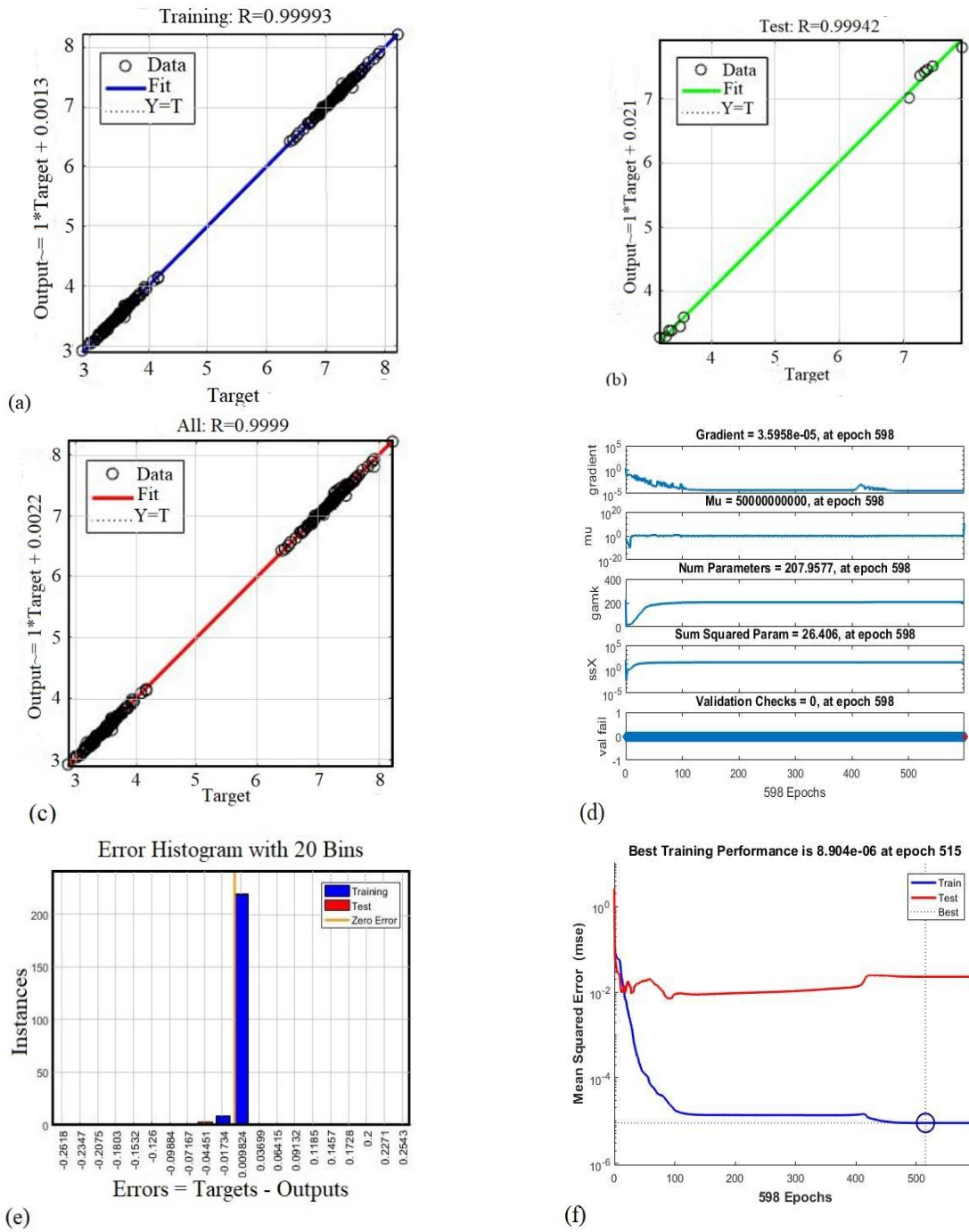


Fig. 8 ANN performance based on multi-objective optimization for: (a) Training data; (b) Test data; (c) All data; (d) Training state; (e) Error histogram; (f) Best training performance

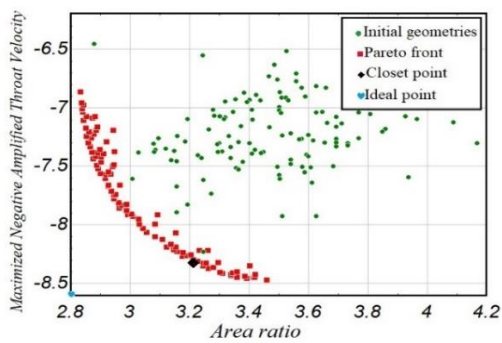


Fig. 9 Initial geometries, pareto front, ideal point and the closest point to the ideal in multi-objective optimization

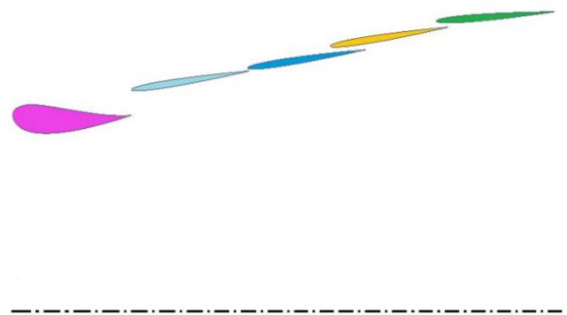


Fig. 10 Optimized geometry of multi objective GA

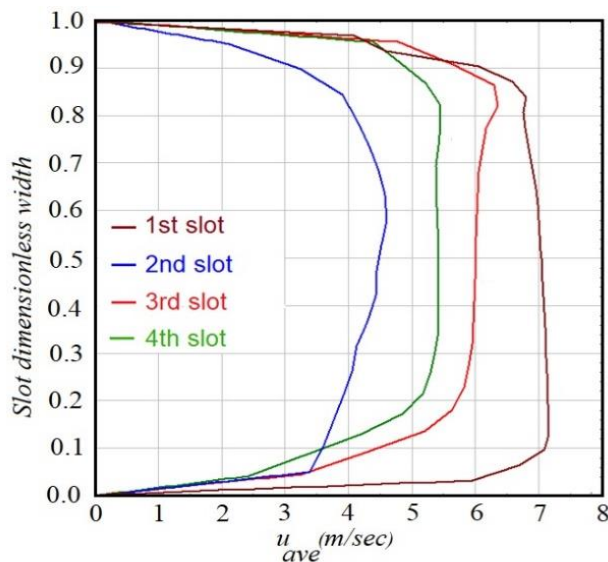


Fig. 11 Profile of the input velocity entering the four slots in the single-objective GA optimization geometry

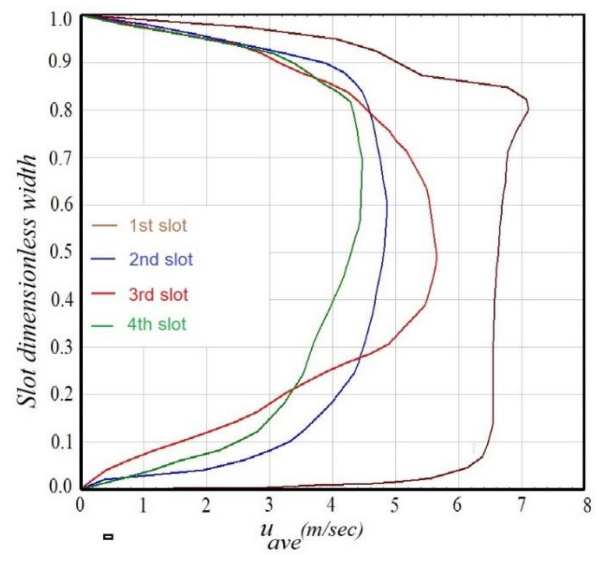


Fig. 12 Profile of the input velocity to the four slots in the geometry of multi-objective GA optimization

The accuracy of the results obtained from the GA optimization is entirely dependent on the accuracy of the function obtained from the ANN. The training process should continue until the closest regression function R and the minimum value for the MSE are obtained to achieve desirable results. According to Fig. 5 and Fig. 8, the value of R in using the single-objective GA optimization for the ANN is 0.99689, and for the multi-objective optimization, it is 0.9999.

By optimizing the nozzle geometries, it is possible to increase the nozzle kinetic energy rate to more than the free stream flow energy rate at the exit plane of the nozzle. According to Table 3 of this study, in the optimized geometry in the single-objective GA for maximum throat velocity and minimum area ratio, the nozzle kinetic energy rate is about 40.4% higher than the free stream flow energy rate at the hypothetical exit plane. Based on the multi-objective GA, this increase in the energy rate is approximately 52.4%, according to the results in Table 6 of the optimized nozzle.

In the GA optimization, for increased efficiency, not all the theoretical capacity increase in the surface area ratio has been utilized to enhance the efficiency of the diffuser.

Contrary to the theory that increasing the area ratio leads to higher efficiency, what happens in practice is that increasing the area ratio beyond a specific limit, due to the adverse effects of positive pressure gradient in the divergent section, flow separation occurs, and the efficiency of the diffuser decreases. Considering the results obtained from the ANN and the single-objective genetic optimization algorithm, and based on the geometric information in Table 2, the maximum area ratio reached 3.810 (see Table 3). Additionally, in multi-objective optimization with the geometric input information in Table 5, the range of area ratio in the optimal states on the Pareto front reached a maximum of 3.5. In the best case (the closest point to the ideal point)

according to Table 6, this area ratio was only 3.205. This is in contrast to the theoretical principles and the constraints on design parameters, where these ratios could have been a maximum of 4. These imposed constraints on the geometry's area ratios in the optimal designs are due to flow control.

The majority of the mass flow entering the boundary layer is from the first slot located between the main diffuser and the first the BLC. According to Table 4, in the diffuser geometry obtained from single-objective GA optimization, approximately 47% of the boundary layer control flow enters from the first gap. Similarly, according to the information in Table 7 about the diffuser optimized by the multi-objective genetic algorithm, this ratio is even higher, reaching about 72%. Also, as shown in Fig. 11 and 12, the average velocity in the first slot is higher than the other gaps. Therefore, the majority of the kinetic energy and momentum injected into the boundary layer comes from the first slot.

Considering the Reynolds number and based on the velocity profiles in Fig. 11 and 12, which belong to the multi-objective optimized geometry, the incoming flows to the boundary layer are turbulent. These flows have more momentum and are more effective in injecting energy into the low-energy boundary layer flow. The increased turbulence and the proximity of the velocity profile to an almost flat state, especially in the 1st slot of the separated flow, means that the main effect on the internal boundary layer of the diffuser occurs from this slot.

As anticipated, injecting a high-energy flow, not only halts internal return flows but also prevents flow separation. The streamlines near the diffuser wall become organized and directed towards the desired direction leading to the exit. In Fig. 13, the streamlines of a short diffuser are presented, having a similar area ratio compared to the diffuser optimized with a single-objective genetic algorithm. Figure 13 illustrates the formation of several separation flows inside the diffuser, creating

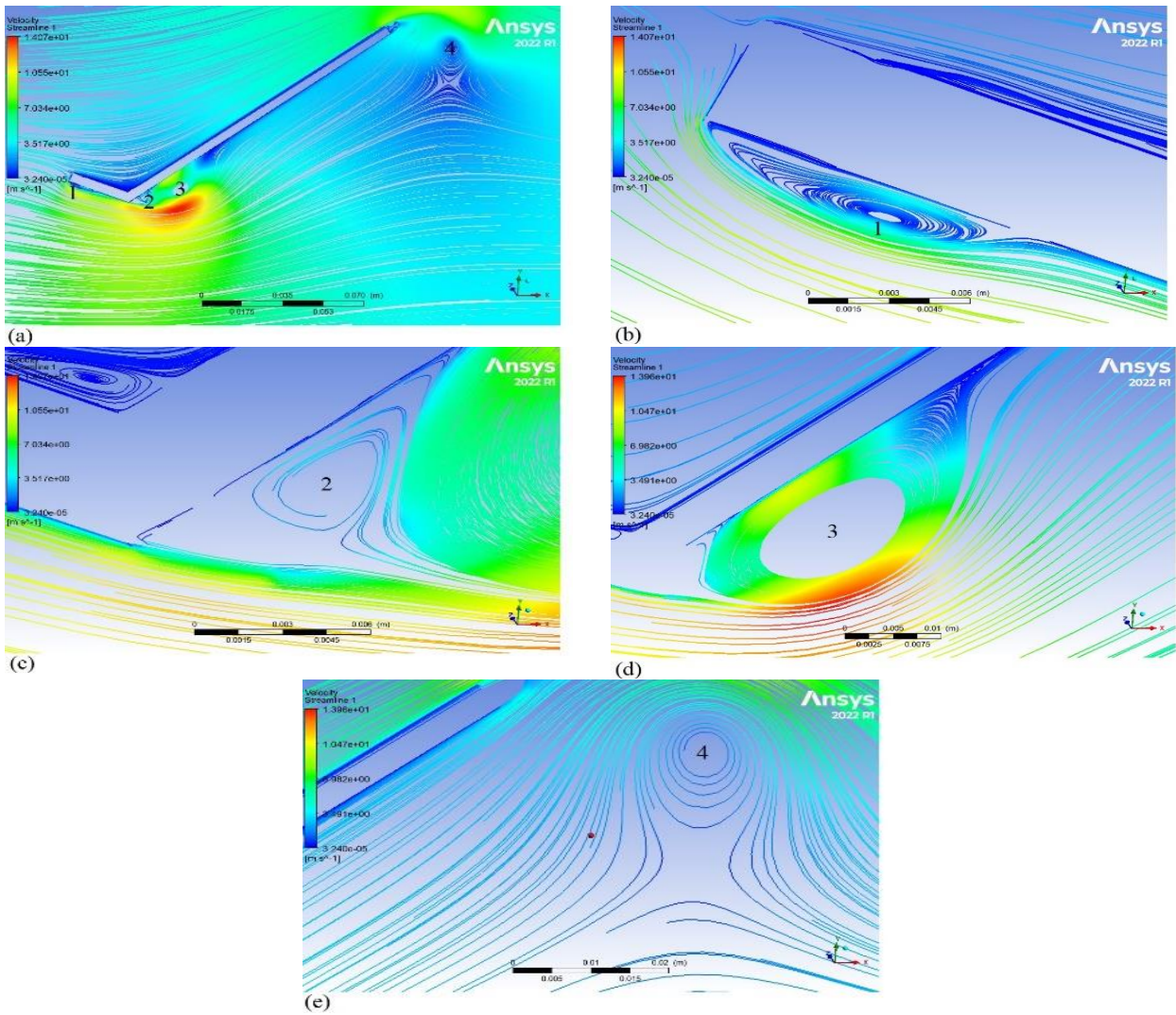


Fig. 13 Streamlines in the short CD diffuser: (a) All domain; (b) Beginning of the Convergent Section; (c) Beginning of the diverging section; (d) Divergent section; (e) After the diffuser

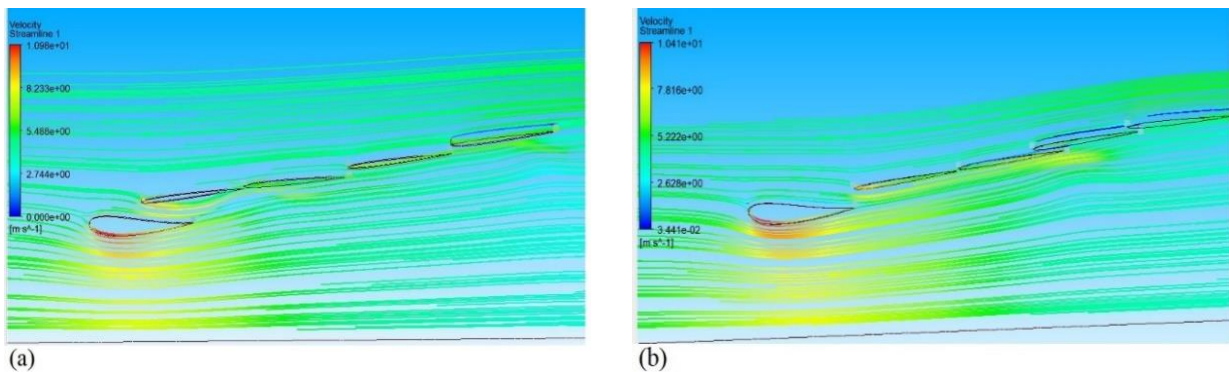


Fig. 14 Streamlines in the optimized BLC diffusers, a) Single objective, b) Multi objective

significant obstacles against flow exit. A comparison of the streamlines of a short converging-diverging diffuser (Fig. 13) with the streamlines of the geometry optimized with the genetic algorithm (Fig. 14) highlights substantial differences in performance.

As mentioned, a range of desirable points is available in the Pareto front in multi-objective optimization. The choice of which optimal design point to use depends on

the application. The upper part of the Pareto homographic chart is related to minimum surfaces and, at the same time, relatively acceptable throat velocity. The lower parts of the chart show higher enhanced velocities and, of course, higher area ratios. Generally, the best design point on the Pareto front is the closest point to the coordinate origin or the ideal point, which is used here as the final geometry and is indicated by in Fig. 9

Optimization with the GA suggests a geometry with higher efficiency compared to the multi-objective GA (comparison of Table 3 and Table 6). This is because in the GA, only one objective is considered, and besides the constraints of the initial design variables, there are no other constraints for optimization. While in the multi-objective optimization GA, in addition to the mentioned constraints, parameters may conflict with each other in optimization, so optimization in this case is done under special conditions.

6. CONCLUSION

This study investigated the design, numerical analysis, and optimization of a multi-slot diffuser geometry with boundary layer control. These multi-slot diffusers, by applying boundary layer control in the positive gradient section, prevent flow separation and significantly increase energy extraction in the diffuser throat, showcasing their potential for enhancing the power of small wind turbines. In each set of diffusers, four boundary layer control diffusers are positioned adjacent to the main diffuser, with geometric parameters such as divergence angle, axial overlap, and radial spacing selected randomly, resulting in a total of 120 different geometries. These geometries were sketched in SolidWorks software and subsequently analyzed through three-dimensional simulations in ANSYS Fluent, yielding results such as average throat velocity and the exit-to-throat area ratio for each configuration.

The outputs from these numerical analyses were input into an artificial neural network (ANN), and the fitted output function was separately introduced to single-objective and multi-objective genetic algorithms (GAs) to achieve two optimized geometries. Key findings of this study are as follows:

- **High accuracy of GA optimization results:** Due to the high accuracy of the R-value in the ANN fitting function, the GA optimization results exhibit high precision. The R-value is 0.99689 in single-objective optimization and 0.9999 in multi-objective optimization, indicating the quality of ANN training.
- **Validation of the three-dimensional numerical solution:** To verify the accuracy of the numerical settings, a portion of the two-dimensional numerical results (Kishore et al., 2013) was validated in a three-dimensional solution. The relative difference percentage (RPD) between the two-dimensional and three-dimensional results was approximately 2.3%, which is negligible and acceptable for comparing two- and three-dimensional solutions.
- **Advantages of ANN and GA in the optimization process:** In this study, ANN and GA were utilized effectively as a substitute for the gradient descent method, which is time-intensive. This approach enabled optimization with only 120 geometries, eliminating the need for gradual and time-consuming exploration of additional designs. The

comparison between the numerically solved optimized geometries and the predicted optimized geometries from ANN and GA demonstrated a satisfactory match. The RPD in multi-objective optimization was around 1.6, and in single-objective optimization, it was approximately 2.1, indicating the efficiency of this optimization method.

- **Impact of constrained geometric parameters:** By applying specific constraints on the range of diffuser geometric parameters, the exit-to-throat area ratio was maintained below 4. Despite these constraints, the single-objective GA optimization yielded a geometry where the kinetic energy ratio in the diffuser throat was more than 5.3 times the free-stream kinetic energy ratio, and about 40% higher than the free-stream kinetic energy ratio at the diffuser exit.
- **Prioritization of the first slot in boundary layer control:** The first slot, located between the main diffuser and the first boundary layer control diffuser, plays a critical role. Results indicate that in the diffuser optimized by the single-objective GA, approximately 47% of the boundary layer control flow is injected from the first slot, while in the diffuser optimized by the multi-objective GA, mass flow through the first slot reaches about 72% of the boundary layer control flow.

The findings of this study suggest that boundary layer control and multi-slot diffuser geometry optimization hold significant potential for enhancing the performance of small-scale diffusers for wind turbines. These designs, with their time efficiency and high precision, can serve as an effective approach in wind energy generation technologies.

CONFLICT OF INTEREST

The authors declare that they have no known competing financial interests or personal relationships.

AUTHORS CONTRIBUTION

A. Naghavi Moghaddam: Conceptualization, Data Curation, Formal Analysis, Investigation, Methodology, Resources, Software, Validation, Writing - original draft, Writing - review & editing. **S. M. Malekjafarin:** Conceptualization, Data Curation, Formal Analysis, Investigation, Methodology, Project Administration, Software, Supervision, Validation, Writing - original draft, Writing - review & editing. **S. A. Mirbozorgi:** Conceptualization, Investigation, Methodology, Validation, Writing - review & editing. **A. Bak Khoshnevis:** Investigation, Methodology, Resources, Writing - review & editing.

REFERENCES

- Abe, K., Kihara, H., Sakurai, A., Wada, E., Sato, K., Nishida, M., & Ohya, Y. (2006). An experimental study of tip-vortex structures behind a small wind

- turbine with a flanged diffuser. *Wind & structures*, 9(5), 413-417. <https://scienceon.kisti.re.kr/srch/selectPORSrchArticle.do?cn=JAKO200621349899175>
- Abe, K., Nishida, M., Sakurai, A., Ohya, Y., Kihara, H., Wada, E., & Sato, K. (2005). Experimental and numerical investigations of flow fields behind a small wind turbine with a flanged diffuser. *Journal of Wind Engineering and Industrial Aerodynamics*, 93(12), 951-970. <https://doi.org/https://doi.org/10.1016/j.jweia.2005.09.003>
- Ackermann, T., & Söder, L. (2002). An overview of wind energy-status 2002. *Renewable and Sustainable Energy Reviews*, 6(1), 67-127. [https://doi.org/https://doi.org/10.1016/S1364-0321\(02\)00008-4](https://doi.org/https://doi.org/10.1016/S1364-0321(02)00008-4)
- Agha, A., Chaudhry, H. N., & Wang, F. (2018). Diffuser Augmented Wind Turbine (DAWT) technologies: A review. *International Journal of Renewable Energy Research*, 8(3), 1369-1385. <https://doi.org/10.20508/ijrer.v8i3.7794.g7436>
- Agha, A., Chaudhry, H. N., & Wang, F. (2020). Determining the augmentation ratio and response behaviour of a Diffuser Augmented Wind Turbine (DAWT). *Sustainable Energy Technologies and Assessments*, 37, 100610. <https://doi.org/https://doi.org/10.1016/j.seta.2019.100610>
- Ahmed, A. S. (2010). Wind energy as a potential generation source at Ras Benas, Egypt. *Renewable and Sustainable Energy Reviews*, 14(8), 2167-2173. <https://doi.org/https://doi.org/10.1016/j.rser.2010.03.006>
- Alquraishi, B. A., Asmuin, N. Z., Mohd, S., Abd Al-Wahid, W. A., & Mohammed, A. N. (2019). Review on diffuser augmented wind turbine (dawt). *International Journal of Integrated Engineering*, 11(1). <http://penerbit.uthm.edu.my/ojs/index.php/ijie>
- Behzadian, K., Kapelan, Z., Savic, D., & Ardeshtir, A. (2009). Stochastic sampling design using a multi-objective genetic algorithm and adaptive neural networks. *Environmental Modelling & Software*, 24(4), 530-541. <https://doi.org/https://doi.org/10.1016/j.envsoft.2008.09.013>
- Ben David Wood, O. G. (2014). *Diffuser Augmented Wind Turbines*. US Patent number: 9,512,817 B2 <https://www.patents-review.com/a/20140227092-diffuser-augmented-wind-turbines.html>
- Bode, F., Meslem, A., Patrascu, C., & Nastase, I. (2020). Flow and wall shear rate analysis for a cruciform jet impacting on a plate at short distance. *Progress in Computational Fluid Dynamics, an International Journal*, 20(3), 169-185. <https://doi.org/10.1504/PCFD.2020.107276>
- Bontempo, R., Carandente, R., & Manna, M. (2021). A design of experiment approach as applied to the analysis of diffuser-augmented wind turbines. *Energy Conversion and Management*, 235, 113924. <https://doi.org/https://doi.org/10.1016/j.enconman.2021.113924>
- Dighe, V. V., Avallone, F., Igra, O., & van Bussel, G. (2019). Multi-element ducts for ducted wind turbines: a numerical study. *Wind Energy Science*, 4(3), 439-449. <https://doi.org/10.5194/wes-4-439-2019>
- Dighe, V. V., de Oliveira, G., Avallone, F., & van Bussel, G. J. W. (2018). *On the effects of the shape of the duct for ducted wind turbines*. 2018 Wind Energy Symposium. American Institute of Aeronautics and Astronautics. <https://doi.org/doi:10.2514/6.2018-0997>
- Ding, C., Zhang, B., Liang, C., Visser, K., & Yao, G. (2022). High-Order Large eddy simulations of a wind turbine in ducted and open-rotor configurations. *Journal of Fluids Engineering*, 145(2). <https://doi.org/10.1115/1.4055989>
- Dong, Y., Li, Z., & Li, J. (2023). Investigations on the splitter structure to improve the aerodynamic performance of gas turbine exhaust diffuser at different swirl angles. *Journal of Engineering for Gas Turbines and Power*, 145(6). <https://doi.org/10.1115/1.4056428>
- Eriksson, K., Ramasamy, S., Zhang, X., Wang, Z., & Danielsson, F. (2022). Conceptual framework of scheduling applying discrete event simulation as an environment for deep reinforcement learning. *Procedia CIRP*, 107, 955-960. <https://doi.org/https://doi.org/10.1016/j.procir.2022.05.091>
- García Auyanet, A., & Verdin, P. G. (2022). Numerical study of the effect of flap geometry in a multi-slot ducted wind turbine. *Sustainability*, 14(19), 12032. <https://doi.org/10.3390/su141912032>
- Ghajar, R. F., & Badr, E. A. (2008). An experimental study of a collector and diffuser system on a small demonstration wind turbine. *International Journal of Mechanical Engineering Education*, 36(1), 58-68. <https://doi.org/10.7227/IJMEE.36.1.6>
- Gilbert, B. L., & Foreman, K. M. (1979). Experimental demonstration of the diffuser-augmented wind turbine concept. *Journal of Energy*, 3(4), 235-240. <https://doi.org/10.2514/3.48002>
- Gilbert, B. L., & Foreman, K. M. (1983). Experiments with a diffuser-augmented model wind turbine. *Journal of Energy Resources Technology*, 105(1), 46-53. <https://doi.org/10.1115/1.3230875>
- Goldberg, U. C., & Batten, P. (2015). A wall-distance-free version of the SST turbulence model. *Engineering Applications of Computational Fluid Mechanics*, 9(1), 33-40. <https://doi.org/10.1080/19942060.2015.1004791>
- Heyru, B., & Bogale, W. (2022). Flow field analysis and testing of curved shroud wind turbine with different flange angle. *Cogent Engineering*, 9(1), 2095951.

- Hjort, S., & Larsen, H. (2014). A Multi-Element Diffuser Augmented Wind Turbine. *Energies*, 7(5), 3256-3281. <https://www.mdpi.com/1996-1073/7/5/3256>
- Hornik, K., Stinchcombe, M., & White, H. (1989). Multilayer feedforward networks are universal approximators. *Neural Networks*, 2(5), 359-366. [https://doi.org/https://doi.org/10.1016/0893-6080\(89\)90020-8](https://doi.org/https://doi.org/10.1016/0893-6080(89)90020-8)
- Igra, O. (1981). Research and development for shrouded wind turbines. *Energy Conversion and Management*, 21(1), 13-48. [https://doi.org/https://doi.org/10.1016/0196-8904\(81\)90005-4](https://doi.org/https://doi.org/10.1016/0196-8904(81)90005-4)
- Jafari, S. A. H., & Kosasih, B. (2014). Flow analysis of shrouded small wind turbine with a simple frustum diffuser with computational fluid dynamics simulations. *Journal of Wind Engineering and Industrial Aerodynamics*, 125, 102-110. <https://doi.org/https://doi.org/10.1016/j.jweia.2013.12.001>
- Kishore, R. A., Coudron, T., & Priya, S. (2013). Small-scale wind energy portable turbine (SWEPT). *Journal of Wind Engineering and Industrial Aerodynamics*, 116, 21-31. <https://doi.org/https://doi.org/10.1016/j.jweia.2013.01.010>
- Koc, E., & Yavuz, T. (2019). Effect of flap on the wind turbine-concentrator combination. *International Journal of Renewable Energy Research (IJRER)*, 9(2), 551-560. <https://doi.org/10.20508/ijrer.v9i2.8838.g7625>
- Konak, A., Coit, D. W., & Smith, A. E. (2006). Multi-objective optimization using genetic algorithms: A tutorial. *Reliability Engineering & System Safety*, 91(9), 992-1007. <https://doi.org/https://doi.org/10.1016/j.res.2005.11.018>
- Kwong, A. H., & Dowling, A. P. (1994). Active boundary-layer control in diffusers. *AIAA journal*, 32(12), 2409-2414. <https://doi.org/10.2514/3.12307>
- Lawn, C. J. (2003). Optimization of the power output from ducted turbines. *Proceedings of the Institution of Mechanical Engineers, Part A: Journal of Power and Energy*, 217(1), 107-117. <https://doi.org/10.1243/095765003321148754>
- Li, S., Wunsch, D. C., O'Hair, E., & Giesselmann, M. G. (2001). Comparative Analysis of regression and artificial neural network models for wind turbine power curve estimation. *Journal of Solar Energy Engineering*, 123(4), 327-332. <https://doi.org/10.1115/1.1413216>
- Lilley, G., & Rainbird, W. (1956). A preliminary report on the design and performance of ducted windmills.
- Loeffler Jr, A. L. (1981). Flow Field Analysis and Performance of Wind Turbines Employing Slotted Diffusers. *Journal of Solar Energy Engineering*, 103(1), 17-22. <https://doi.org/10.1115/1.3266198>
- Magdi, R., & Adam, M. R. (2011). Wind turbines theory - the betz equation and optimal rotor tip speed ratio. In C. Rupp (Ed.), *Fundamental and advanced topics in wind power* (pp. Ch. 2). IntechOpen. <https://doi.org/10.5772/21398>
- Mei, Z., Gao, B., Zhang, N., Lai, Y., & Li, G. (2022). Numerical Study on the unsteady flow field characteristics of a podded propulsor based on DDES method. *Energies*, 15(23), 9117. <https://www.mdpi.com/1996-1073/15/23/9117>
- Menter, F. R. Kuntz, M., & Langtry, R. (2003). Ten Years of Industrial Experience with the SST Turbulence Model. In K. Hanjalic, Y. Nagano, & M. Tummers (Eds.), *Proceedings of the 4th International Symposium on Turbulence, Heat and Mass Transfer* (pp. 625-632). Begell House
- Menter, F. R. (1994). Two-equation eddy-viscosity turbulence models for engineering applications. *AIAA Journal*, 32(8), 1598-1605. <https://doi.org/10.2514/3.12149>
- Mohammed, A., Mohd Khairul Hafiz, M., Faizal, M., Kamarul Arifin, A., & Noorfaizal, Y. (2022). Design of wind nozzle for nozzle augmented wind turbine. *Journal of Advanced Research in Fluid Mechanics and Thermal Sciences*, 95(1), 36-43. <https://doi.org/10.37934/arfmts.95.1.3643>
- Ohya, Y., & Karasudani, T. (2010). A Shrouded wind turbine generating high output power with wind-lens technology. *Energies*, 3(4), 634-649. <https://www.mdpi.com/1996-1073/3/4/634>
- Ohya, Y., Karasudani, T., Sakurai, A., Abe, K. I., & Inoue, M. (2008). Development of a shrouded wind turbine with a flanged diffuser. *Journal of Wind Engineering and Industrial Aerodynamics*, 96(5), 524-539. <https://doi.org/https://doi.org/10.1016/j.jweia.2008.01.006>
- Oman, R. A., Foreman, K. M., & Gilbert, B. L. (1976a). *Investigation of diffuser-augmented wind turbines*. <https://ui.adsabs.harvard.edu/abs/1976gac..rept....O>
- Oman, R., Foreman, K., & Gilbert, B. (1976b). *Investigation of diffuser-augmented wind turbines. Progress Report*.
- Pajasmaa, J. Miettinen, K. & Silvennoinen, J. Group Decision Making in Multiobjective Optimization: A Systematic Literature Review. *Group Decis Negot* (2024). <https://doi.org/10.1007/s10726-024-09915-8>
- Panwar, N. L., Kaushik, S. C., & Kothari, S. (2011). Role of renewable energy sources in environmental protection: A review. *Renewable and Sustainable Energy Reviews*, 15(3), 1513-1524. <https://doi.org/https://doi.org/10.1016/j.rser.2010.11.037>
- Perlin, M., Dowling, D. R., & Ceccio, S. L. (2016). Freeman scholar review: passive and active skin-friction drag reduction in turbulent boundary layers. *Journal of Fluids Engineering*, 138(9). <https://doi.org/10.1115/1.4033295>

- Phillips, D. G. (2003). *An investigation on diffuser augmented wind turbine design* University of Auckland.
<https://books.google.com/books?id=v266NwAACAAJ>
- Phillips, D. G., Flay, R. G. J., & Nash, T. A. (1999). Aerodynamic Analysis and monitoring of the vortec 7 diffuser-augmented wind turbine. *Transactions of the Institution of Professional Engineers New Zealand: Electrical/Mechanical/Chemical Engineering Section*, 26(1), 13-19.
<https://search.informit.org/doi/10.3316/informit.290017493057769>
- Promthaisong, P., & Eiamsa-ard, S. (2019). Fully developed periodic and thermal performance evaluation of a solar air heater channel with wavy-triangular ribs placed on an absorber plate. *International Journal of Thermal Sciences*, 140, 413-428.
<https://doi.org/https://doi.org/10.1016/j.ijthermalsci.2019.03.010>
- Rahman, M. M., Vuorinen, V., Taghinia, J., & Larimi, M. (2019). Wall-distance-free formulation for SST k- ω model. *European Journal of Mechanics - B/Fluids*, 75, 71-82.
<https://doi.org/https://doi.org/10.1016/j.euromechflu.2018.11.010>
- Ramayee, L., & Supradeepan, K. (2022). Influence of axial distance and duct angle in the improvement of power generation in duct augmented wind turbines. *Journal of Energy Resources Technology*, 144(9).
<https://doi.org/10.1115/1.4053615>
- Ramesh Kumar, K., & Selvaraj, M. (2023). Novel deep learning model for predicting wind velocity and power estimation in advanced INVELOX wind turbines. *Journal of Applied Fluid Mechanics*, 16(6), 1256-1268. <https://doi.org/10.47176/jafm.16.06.1637>
- Ranjbar, M. H., Mashouf, H., Gharali, K., Rafiei, B., Al-Haq, A., & Nathwani, J. (2022). Power augmentation of ducted wind turbines for urban structures: Experimental, numerical, and economic approaches. *Energy Science & Engineering*, 10(10), 3893-3907.
<https://doi.org/https://doi.org/10.1002/ese3.1252>
- Ruprecht, A., & Reinhardt, H. (2003). Development of a Maritime Current Turbine. *Proceedings of the ASME/JSME 2003 4th Joint Fluids Summer Engineering Conference*. Volume 1: Fora, Parts A, B, C, and D. Honolulu, Hawaii, USA. July 6–10, 2003. pp. 1871-1876. ASME.
<https://doi.org/10.1115/FEDSM2003-45683>
- Schmitt, L. M. (2001). Theory of genetic algorithms. *Theoretical Computer Science*, 259(1), 1-61.
[https://doi.org/https://doi.org/10.1016/S0304-3975\(00\)00406-0](https://doi.org/https://doi.org/10.1016/S0304-3975(00)00406-0)
- Seeni, A. (2019). Numerical validation of NACA 0009 airfoil in ultra-low reynolds number flows. *International Review of Aerospace Engineering*, 12, 83-92.
- Shahsavari, M., Bibeau, E. L., & Chatoorgoon, V. (2015). Effect of shroud on the performance of horizontal axis hydrokinetic turbines. *Ocean Engineering*, 96, 215-225.
<https://doi.org/10.1016/j.oceaneng.2014.12.006>
- Siavash, N. K., Ghobadian, B., Najafi, G., Rohani, A., Tavakoli, T., Mahmoodi, E., Mamat, R., & mazlan, M. (2021). Prediction of power generation and rotor angular speed of a small wind turbine equipped to a controllable duct using artificial neural network and multiple linear regression. *Environmental Research*, 196, 110434.
<https://doi.org/https://doi.org/10.1016/j.envres.2020.110434>
- Tacutu, L., Nastase, I., Bode, F., Croitoru, C., & Lungu, C. (2019). *Numerical models development for unidirectional air flow diffusers with lobed and circular orifices*. E3S Web of Conferences, 111, 01049.
<https://doi.org/10.1051/e3sconf/201911101049>
- Thangavelu, S. K., Mutasher, S., & Lau, Y. (2013). Design and flow velocity simulation of diffuser augmented wind turbine using CFD. *Journal of Engineering Science and Technology*, 8, 372-384.
- Tripathi, S. K. (2017). Performance Analysis of diffuser augmented horizontal axis wind turbine. *International Journal of Approximate Reasoning*, 5, 1251-1259.
<https://doi.org/10.21474/IJAR01/4240>
- Van Bussel, G. J. (2007). *The science of making more torque from wind: Diffuser experiments and theory revisited*. Journal of Physics: Conference Series.
- Vaz, J. R. P., & Wood, D. H. (2018). Effect of the diffuser efficiency on wind turbine performance. *Renewable Energy*, 126, 969-977.
<https://doi.org/https://doi.org/10.1016/j.renene.2018.04.013>
- Wilson, R. E. (1980). Wind-turbine aerodynamics. *Journal of Wind Engineering and Industrial Aerodynamics*, 5(3), 357-372.
[https://doi.org/https://doi.org/10.1016/0167-6105\(80\)90042-2](https://doi.org/https://doi.org/10.1016/0167-6105(80)90042-2)
- Yadegari, M. (2021). An optimal design for S-shaped air intake diffusers using simultaneous entropy generation analysis and multi-objective genetic algorithm. *The European Physical Journal Plus*, 136(10), 1019.
<https://doi.org/10.1140/epjp/s13360-021-01999-4>
- Yadegari, M., & Bak Khoshnevis, A. (2020a). Entropy generation analysis of turbulent boundary layer flow in different curved diffusers in air-conditioning systems. *European Physical Journal Plus*, 135(6).
<https://doi.org/10.1140/epjp/s13360-020-00545-y>
- Yadegari, M., & Bak Khoshnevis, A. (2020b). Numerical study of the effects of adverse pressure gradient parameter, turning angle and curvature ratio on turbulent flow in 3D turning curved rectangular diffusers using entropy generation analysis. *The European Physical Journal Plus*, 135(7), 548.
<https://doi.org/10.1140/epjp/s13360-020-00561-y>

- Yadegari, M., & Bak Khoshnevis, A. (2020c). A numerical study over the effect of curvature and adverse pressure gradient on development of flow inside gas transmission pipelines. *Journal of the Brazilian Society of Mechanical Sciences and Engineering*, 42(8), 413. <https://doi.org/10.1007/s40430-020-02495-z>
- Yadegari, M., & Bak Khoshnevis, A. (2021). Investigation of entropy generation, efficiency, static and ideal pressure recovery coefficient in curved annular diffusers. *The European Physical Journal Plus*, 136(1), 69. <https://doi.org/10.1140/epjp/s13360-021-01071-1>
- Zhang, Q., & Wang, X. (2023). Numerical Investigation of Aerodynamic Performances for NREL 5-MW Offshore Wind Turbine. *Wind*, 3(2), 191-212.
- Zore, K., Sasanapuri, B., Parkhi, G., & Varghese, A. (2019). *Ansys mosaic poly-hexcore mesh for high-lift aircraft configuration*. 21th Annual CFD Symposium. <https://www.researchgate.net/publication/335789150>.